Physica Scripta

INCLUSIVE PUBLISHING TRUSTED SCIENCE

PURPOSE-LED PUBLISHING™

**PAPER** • **OPEN ACCESS**

# Investigating the photocatalytic efficacy of a porous cuprous gallate ($CuGa_2O_4$) thick film

To cite this article: Fatima Huseynzade *et al* 2024 *Phys. Scr.* **99** 125905

View the article online for updates and enhancements.

You may also like

- Generalized stacking fault energies, cleavage energies, ionicity and brittleness of Cu(Al/Ga/In)$Se_2$ and CuGa(S/Se/Te)$_2$
H T Xue, F L Tang, T Gruhn et al.
- Electrodeposited Gallium Alloy Thin Films Synthesized by Solid State Reactions for CIGS Solar Cell
S. Ahmed, K. B. Reuter, Q. Huang et al.
- Solution Growth of $CuGa_xIn_{1-x}Se_2$ from CuSe Solutions
Hideto Miyake, Hiroyuki Ohtake, Koichi Sugiyama et al.

This content was downloaded from IP address 88.255.99.31 on 14/03/2025 at 12:17

Physica Scripta

PAPER

# Investigating the photocatalytic efficacy of a porous cuprous gallate ($CuGa_2O_4$) thick film

**Fatima Huseynzade**[1], **Yesim Akbaba**[1], **Shalima Shawuti**[2] and **Musa Mutlu Can**[1]

[1] Renewable Energy and Oxide Hybrid Systems Laboratory, Department of Physics, Faculty of Science, Istanbul University, Vezneciler, Istanbul, Turkey

[2] n²STAR-Koç University Nanofabrication and Nanocharacterization Center for Scientific and Technological Advanced Research, Koç University, Rumelifeneri Yolu, Sariyer, Istanbul, Turkey

**E-mail:** musamutlucan@gmail.com **and** musa.can@istanbul.edu.tr

**Keywords:** oxide semiconductor, wide band gap, spinel oxide, point defect, metal gallate

OPEN ACCESS

RECEIVED
23 May 2024

REVISED
22 September 2024

ACCEPTED FOR PUBLICATION
16 October 2024

PUBLISHED
30 October 2024

Original content from this work may be used under the terms of the Creative Commons Attribution 4.0 licence.

Any further distribution of this work must maintain attribution to the author(s) and the title of the work, journal citation and DOI.

## Abstract

The study aimed to investigate the photocatalytic activity of porous copper gallate ($CuGa_2O_4$) thick film with significant wall dimensions. The thick film was meticulously fabricated using tape casting systems, with $CuGa_2O_4$ nanoparticles synthesized by Sol–Gel technique and subsequently transformed into gels for the tape casting process. Rietveld refinements were employed to elucidate the crystal structure and lattice parameters of the $CuGa_2O_4$ spinel oxide lattice. Moreover, electronic energy configurations and optical transmittance measurements were acquired through UV-visible spectrophotometry. The correlations between the crystal structure, band gap change and formation of electronic energy levels in relation to the photocatalytic performance of $CuGa_2O_4$ were explored. The comprehensive examination provides valuable insights into the complex interaction between material properties and photocatalytic behavior, offering a nuanced understanding of the potential applications of porous $CuGa_2O_4$ thick films in various technological fields.

## Introduction

Spinel oxides, denoted by the general formula AB2O4, stand out as highly versatile materials for a myriad of technological applications owing to their adjustable wide band gap values. In this formulation, A and B represent metallic cations with valence states of +2 and +3, respectively, forming a crystal lattice in the face-centered cubic structure [1]. Widely explored in technological realms, spinel oxides, with their low surface acidity, robust mechanical strength, chemical stability, photo catalytic activity, high ionic diffusion performance, and magnetic sensitivity, have garnered significant attention [2–6].

Among the spinel oxides, copper gallate ($CuGa_2O_4$) emerges as a particularly promising semiconductor material with photocatalytic properties, gaining increased prominence in recent years. $CuGa_2O_4$ spinel oxide has a bandgap value about 2.5 eV, which make the structure useful in visible range of electromagnetic spectra [7].

$CuGa_2O_4$ spinel oxides exhibit considerable potential in the domain of energy conversion, serving as a photocathode material in photo-electrochemical cells for hydrogen production from water [8, 9]. The enduring stability and durability of $CuGa_2O_4$ under photocatalytic conditions render it an appealing candidate for practical applications. Nevertheless, challenges such as low quantum yield and sluggish charge carrier recombination must be addressed to fully exploit the photocatalytic potential of $CuGa_2O_4$. Additionally, the synthesis of high-quality $CuGa_2O_4$ nanoparticles with controlled size and shape remains a formidable task.

The photocatalytic activity of $CuGa_2O_4$ represents a promising avenue of research with the potential to contribute significantly to the development of sustainable technologies for environmental remediation, seawater electrolysis and energy conversion [10]. Furthermore, the advantages of spinels over other oxide structures like peroxides, the surface reactivity of spinel $CuGa_2O_4$ chemically stable and the photocatalytic performance is independent from the surface cation configuration [11].

© 2024 The Author(s). Published by IOP Publishing Ltd

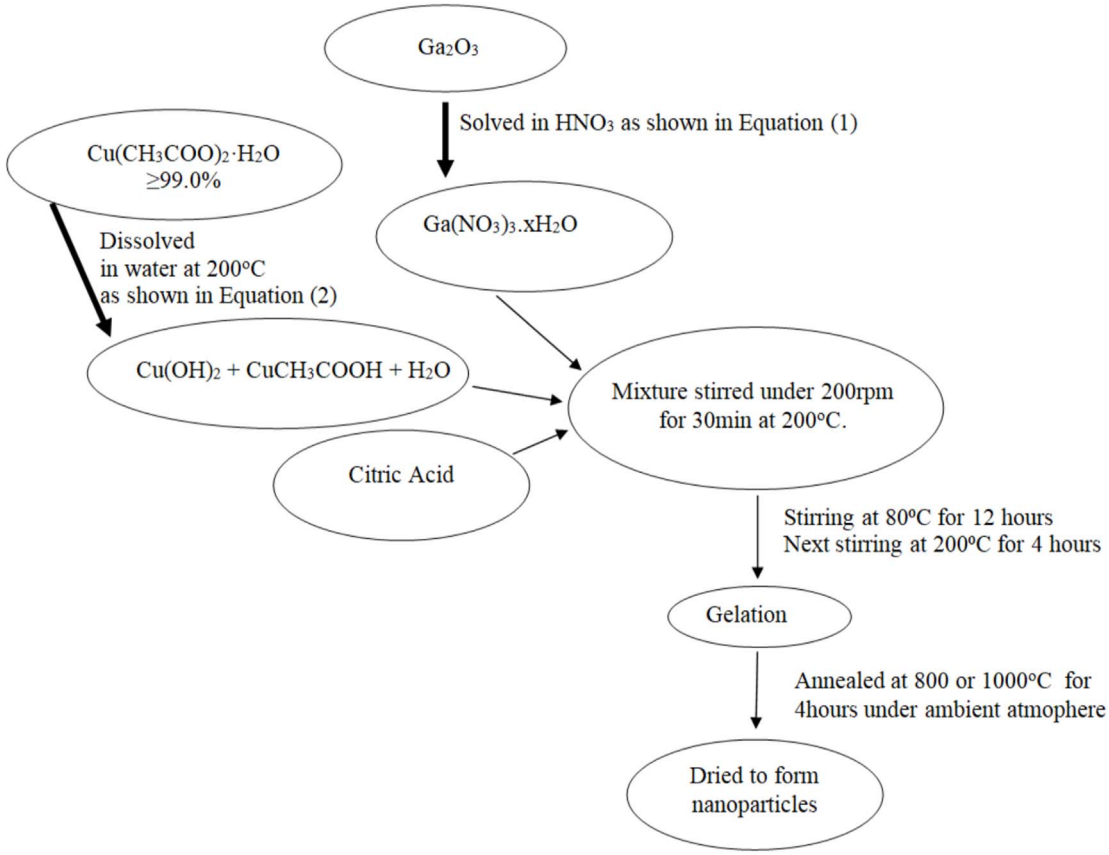


**Figure 1.** Schematic diagram of synthesis of $CuGa_2O_4$ nanoparticles.

Despite existing studies, a comprehensive understanding of the structural, morphological, optical, and electronic properties of $CuGa_2O_4$ as a photocathode material is still lacking in the literature. Overall, it is crucial to prioritize the synthesis of high-quality samples to optimize the photocatalytic activity of $CuGa_2O_4$ for applications in energy conversion.

## Experimental

Sol–gel method was used to obtain $CuGa_2O_4$ nanoparticles. Materials using in the reaction were copper acetate monohydrate ($Cu(CH_3COO)_2{\cdot}H_2O$, ⩾99.0%) and gallium oxide ($Ga_2O_3$, ⩾99.999%). Firstly, gallium oxide was dissolved with water ($H_2O$) and nitric acid ($HNO_3$) under argon gas as shown in chemical reaction of (1) [12]. The solution, obtained in chemical reaction (1), was used directly in the chemical reaction (3) where the recipe was followed for the first time in the synthesis of $CuGa_2O_4$ as far as seen in the literature. Moreover, $Cu(CH_3COO)_2{\cdot}H_2O$ salts was dissolved with water as defined in chemical reaction of (2).

$$Ga_2O_3 + 6HNO_3 + H_2O \rightarrow 2Ga(NO_3)_3 \cdot 4H_2O \quad (1)$$

$$Cu(CH_3COO)_2 \cdot H_2O + H_2O \rightarrow Cu(OH)_2(\text{weak base}) + CH_3COOH(\text{weak acid}) \quad (2)$$

$$Ga_2O_3 + Cu(CH_3COO)_2 \cdot H_2O + C_6H_8O_7 + HNO_3 + H_2O \rightarrow CuGa_2O_4 + X \quad (3)$$

Then, final solutions in chemical reactions of (1) and (2) were mixed with citric acid ($C_6H_8O_7$) as shown in (3). The weight ratio of mixture to $C_6H_8O_7$ was 2:1. Reaction was continued at 200 °C for four hours under argon gas and 200 rpm stirring rate. The process was continued until the gel formed and dried. The sol–gel process was illustrated by schematic diagram in figure 1.

At the end of chemical reaction, shown in figure 1, the mixture was obtained as a gel. And after gelation, three separate annealing processes were performed to the mixture up to at 500 °C, 800 °C and 1000 °C for 2 h in order to get rid of undesired organic molecules such as ethanol, water molecules, unreacted citric acid and weakly bonded functional groups such as hydroxide (COOH) bonded on nanoparticle surfaces [6].

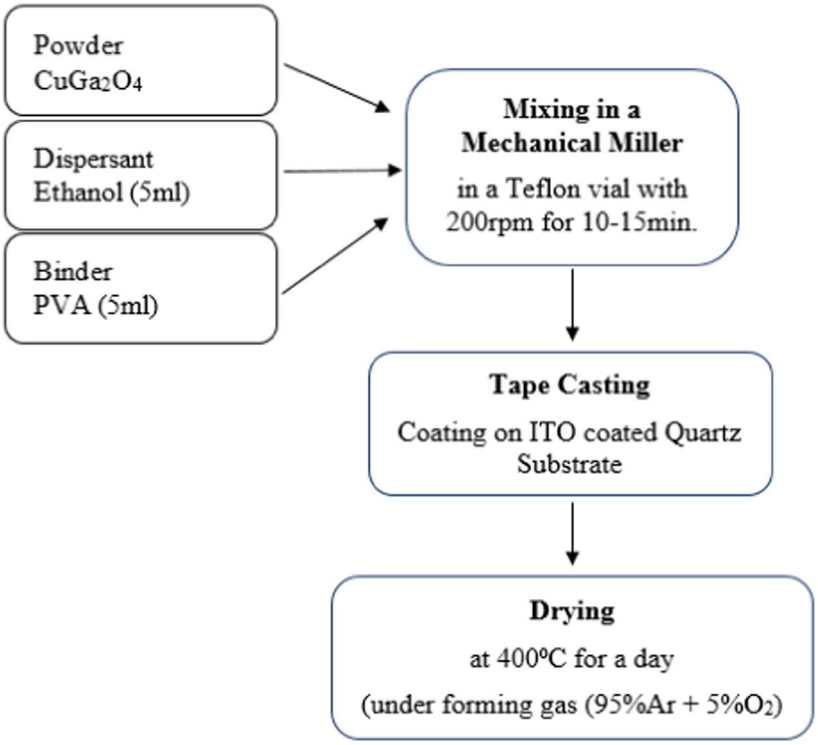


**Figure 2.** Schematic diagram of tape casting procedure.

Then, the synthesized particles were coated on a ITO (indium tin oxide) coated quartz substrates. Coating steps were illustrated by a scheme shown in figure 2. The general recipe in the literature was performed for the gel casting method [13]. Synthesized spinel oxide powders were dispersed in ethanol and mixed with the binder of polyvinyl alcohol (PVA). Then, the mixture was stirred at the rotation speed of 200 rpm for 15 min inside a Teflon vial to mix thoroughly by the Mechanical Miller. The final slurry was used to produce thick film via the Tape Casting system.

Structural analyses were performed employing x-ray powder diffractometer (XRD), transmission electron microscopy (TEM), and x-ray photoelectron spectroscopy (XPS). XRD data were obtained from Rigaku Mini Flex with CuK$\alpha$ radiation in 0.05°/min steps between 10° and 90°. The xrd patterns were employed for Rietveld analyses performed via FULLPROF subprogramme [14]. XPS measurements were taken through Thermo K-alpha x-ray photoelectron spectroscopy which has Al-K$\alpha$ monochromatic x-ray light source with ~0.1 eV resolution. Each XPS spectra was shifted against the electronic charging effect by positioning the C 1 s binding energy peak at 284.5 eV. Right after correction of charging effect, the XPS data was worked out via XPSPEAK41 peak fitting program to identify the oxidation states of cations. TEM measurements were performed for particle size distribution and d-space length measurement. EDS (Oxford X-MaxN) measurements were employed for understanding the cation stoichiometry ratio and elemental analyses.

Band gap values of $CuGa_2O_4$ nanopowders were calculated employing UV–vis. Spectrometer, Shimadzu UV-2600 UV–vis spectrophotometer. The wavelength range of UV–vis. spectra were changed from 220 nm to 1400 nm with 1 nm steps.

## Result and discussion

The samples were produced employing Sol–Gel technique. At the end of chemical route, the mixture was obtained in the gel states. Then, the gel mixtures were annealed at temperature values of 500 °C, 800 °C and 1000 °C for 2 h. No annealing process was performed at the lower temperature values than 500 °C because of possible unreacted citric acid and weakly bonded functional groups such as hydroxide (COOH) or citric acid molecules bonded on nanoparticle surfaces [6]. In order to get rid of unexpected chemicals, samples were annealed at 500 °C or higher values than 500 °C such as 800 °C and 1000 °C. The structural formations were identified by XRD patterns shown in figure 3.

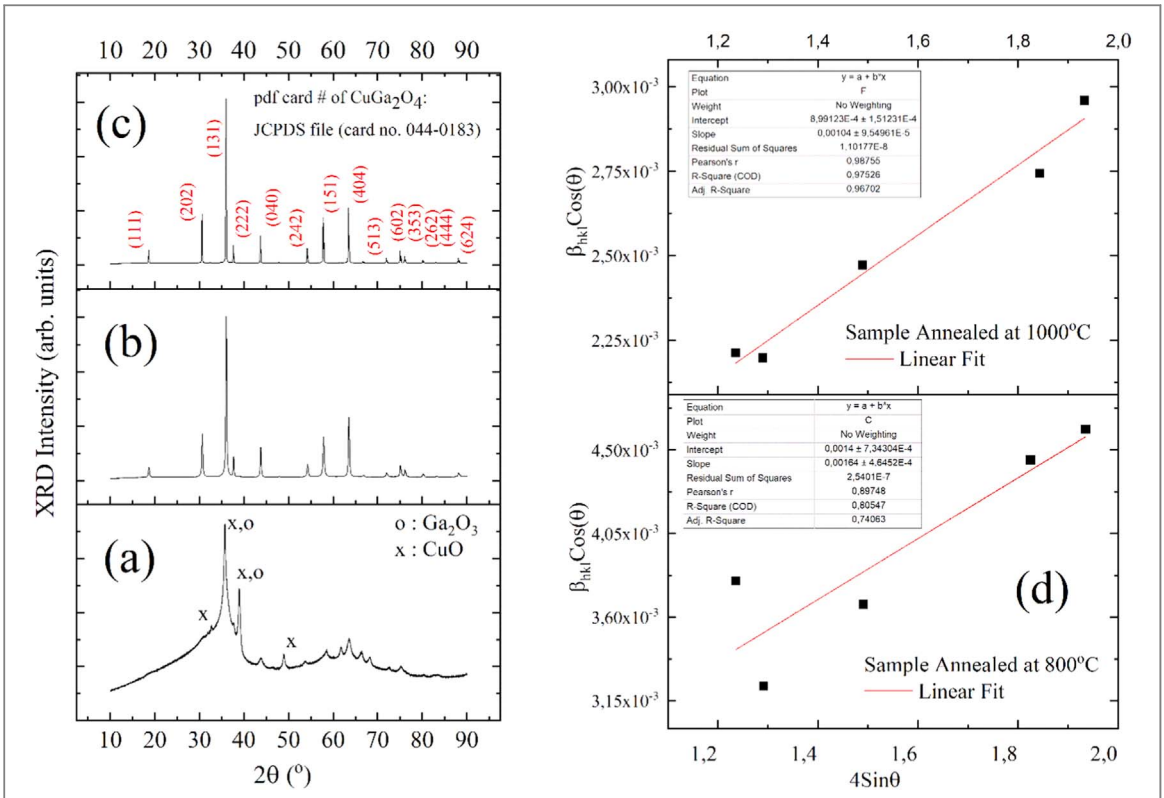


**Figure 3.** The xrd patterns of annealed particles at (a) 500 °C, (b) 800 °C, (c) 1000 °C and (d) fits to Uniform Deformation Model (UDM) for the samples annealed at 800 °C and 1000 °C.

There separate xrd patterns were obtained. On the pattern of sample, obtained at low temperature, was full of unexpected diffraction peaks originating from $Ga_2O_3$ and CuO as identified on the figure [15]. Moreover, high background indicated amorphous phases originating from organic chemical remaining during the chemical route process. No unexpected diffraction peaks were observed in the samples obtained at high annealing temperature values such as 800 °C and 1000 °C. Even though not observing extra peaks, the full width half maximum (FWHM) values of xrd peaks were narrowed after annealing processes. The FWHM values of nanoparticle were correlated with size distribution and microstrain of nanoparticles. High strain value of nanoparticles can be the indicator of broadening XRD peaks [16]. Uniform Deformation Model (UDM), defined by the equation shown in (1), employed to calculate the intrinsic strain [16].

$$\beta_{hkl}\ \mathrm{Cos}\ \theta = \frac{K\lambda}{L} + 4\varepsilon\ \mathrm{Sin}\ \theta \qquad ((1a))$$

FWHM, the average particle sizes, the constant of shape factor (=0.9), the radiation wavelength of CuK$\alpha$ (1.5406 Å), strain and the angle of diffraction were indicated by the symbols of $\beta_{hkl}$, L, K, $\lambda$, $\varepsilon$ and $\theta$, respectively. The fits to Uniform Deformation Model (UDM) for the samples, annealed at 800 °C and 1000 °C, were shown in figure 3(d). the fits were used to calculate the particle and the microstrain of particles.

The decrease in particle sizes and enhanced strain were associated broadening XRD peaks as observed in figure 3(d). The calculations were performed by the diffraction peaks of (131), (222), (040), and (040). The crystallite sizes of samples, annealed at 800 °C and 1000 °C, were found as $99 \pm 2$ nm and $154 \pm 5$ nm, respectively. The average particle size calculations were obtained from the diffraction peaks of (111), (202), (131), (242) and (151). Furthermore, the FWHM values were used for microstrain calculations, $16 \pm 4 \times 10^{-4}$ (800 °C) and $10 \pm 1 \times 10^{-4}$ (1000 °C), by employing equation (1). The micro-strain values showed that annealing at high temperature of 1000 °C caused to form low microstrain, which associated with a lattice dislocation density [17].

The XRD patterns of final products, obtained at 800 °C and 1000 °C, were coherent to JCPDS file PDF card # 044–0183 of $CuGa_2O_4$ crystal structure without diffraction peak of possible impurity crystal phases. Atomic positions in the lattice and lattice parameters of the crystal structures were determined by Rietveld refinement using the FullProf Suite program. The refinements were performed for XRD patterns of particles annealed at 800 °C and 1000 °C. The refinements were calculated for a normal spinel states of $CuGa_2O_4$ crystal structure. Cu

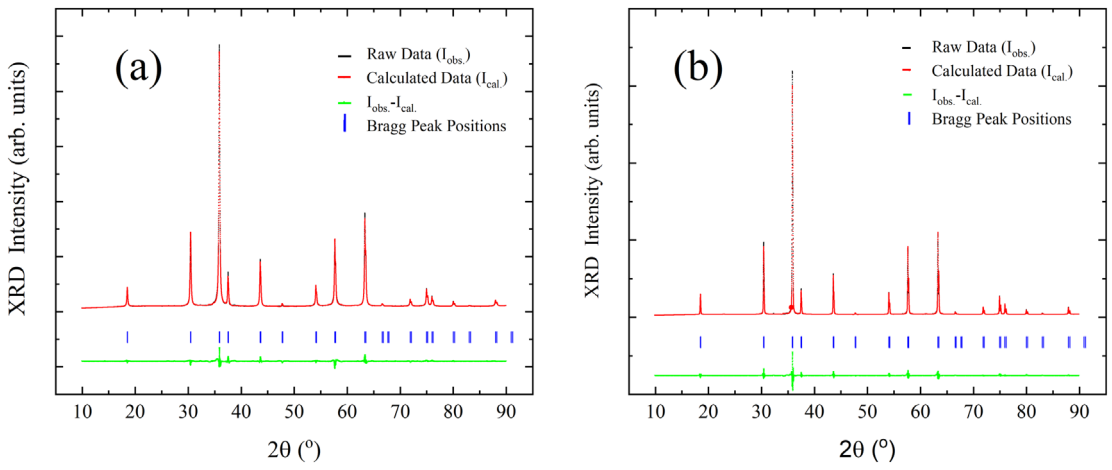


**Figure 4.** Fullprof analyses of $CuGa_2O_4$ particles, annealed at (a) 800 and (b) 1000 °C.

and Ga atoms were settled to the tetrahedral and octahedral side, respectively, in a face centered cubic (FCC) crystal structure with $Fd\bar{3}m$ space group [15, 18]. The located positions of Cu and Ga cations were suggested as $\left(\frac{1}{8}, \frac{1}{8}, \frac{1}{8}\right)$ and $\left(\frac{1}{2}, \frac{1}{2}, \frac{1}{2}\right)$, respectively. The calculations were illustrated in figure 4 and calculated data were shown in table 1.

The binding energy configurations of $CuGa_2O_4$ crystal structure were shown in figures 5(a)–(e). The binding energy levels of Cu 2p, Ga 2p, Ga 3d and O 1s were indicated by the circles in the full spectra, shown in figure 5(a). The peak positions indicated by circles in figure 5(a) were examined in figures 5(b) to (e) in order to determine the ionic valence states and possible bonding situations in the lattice.

The Ga 3d energy levels were fit into two curves. The fits in figure 5(b) was associated with energy levels peak positions of Ga $3d_{5/2}$ and Ga $3d_{3/2}$. The peak maxima of Ga $3d_{5/2}$ and Ga $3d_{3/2}$ energy level were fit to two peaks with having very close peak maximum values at 19.2 eV and 19.4 eV, which was related with ionization states of $Ga^{3+}$ as mentioned for $CuGa_2O_4$ structures [15, 20]. In addition, the Ga 2p energy levels were also analyzed to figure out the Ga atom positions in the lattice. The Ga 2p energy levels were measured by split of two peak levels of Ga $2p_{1/2}$ and Ga $2p_{3/2}$ energy levels, which located at 1144.2 eV and 1117.3 eV, respectively, as illustrated in figure 5(c). The separation energy between these two peaks is about 26.9 eV, assigned the presence of Ga 3+ oxidation states [21, 22].

The Cu 2p energy levels were detected by Cu $2p_{1/2}$, Cu $2p_{3/2}$ and satellite peaks energy levels. Each energy levels, Cu $2p_{1/2}$ and Cu $2p_{3/2}$, were fit to 2 peaks as shown in figure 5(d). The maximum values of the fits were measured at 932.2 eV ($Cu^{1+}$: Cu $2p_{3/2}$), 933.6 eV ($Cu^{2+}$: Cu $2p_{3/2}$), 940.6 eV (satellite peak), 943.0 eV (satellite peak), 951.8 eV ($Cu^{1+}$: Cu $2p_{1/2}$), 953.5 eV ($Cu^{2+}$: Cu $2p_{1/2}$) and 961.2 eV (satellite peak) peak position. Cu $2p_{3/2}$ and Cu $2p_{1/2}$ binding energy peaks maxima of Cu $2p_{3/2}$ and Cu $2p_{1/2}$ binding energy levels were measured at 933.6 eV and 953.5 eV, respectively. The separation value, 19.9 eV, of Cu 2p energy level with satellite peaks at 943.02 eV, 943.0 eV and 961.2 eV were related to the characteristic peak of the spin–orbit splitting, assigned Cu 2+ oxidation states [15, 20, 21, 23, 24]. On the other hand, the low intensive peaks at 932.2 eV and 951.8 eV were revealed Cu $2p_{3/2}$ and Cu$2p_{1/2}$ energy level splits, respectively, of monovalent Cu ions [21, 22, 25].

The O 1s peak, presented in figure 5(e), was split into two peaks using the combination of Gaussian and Lorentzian fitting methods. Fitted peaks at around 530.0 eV and 530.7 eV were associated with metal and oxygen bonds in the lattice, however having two different peaks with very close values indicate oxygen bonds with different valance states of metal ions such as $Cu^{1+}$ and $Cu^{2+}$ [26].

The surface morphology and quantitative analysis of samples were investigated by SEM and EDS measurements shown in figure 6. The EDS measurement values were very close to the stoichiometric ratio of 1:2 (Cu:Ga cations) in $CuGa_2O_4$. The average particle size of samples was 340 ± 20 nm as calculated from SEM micrographs in figure 6. Then, the optical band gap of the samples was determined employing diffuse reflectance spectra versus wavelength curve using UV–visible photo spectroscopy measurements, which converted by Kubelka–Munk method to absorbance spectra as shown in figure 7.

Two broad bands appeared in wavelength range of 300 and 550 nm which were centered at 314.6 nm (338.9 nm) and 473.7 nm (477.4 nm) for the samples annealed at 800 °C (at 1000 °C). The peaks were associated

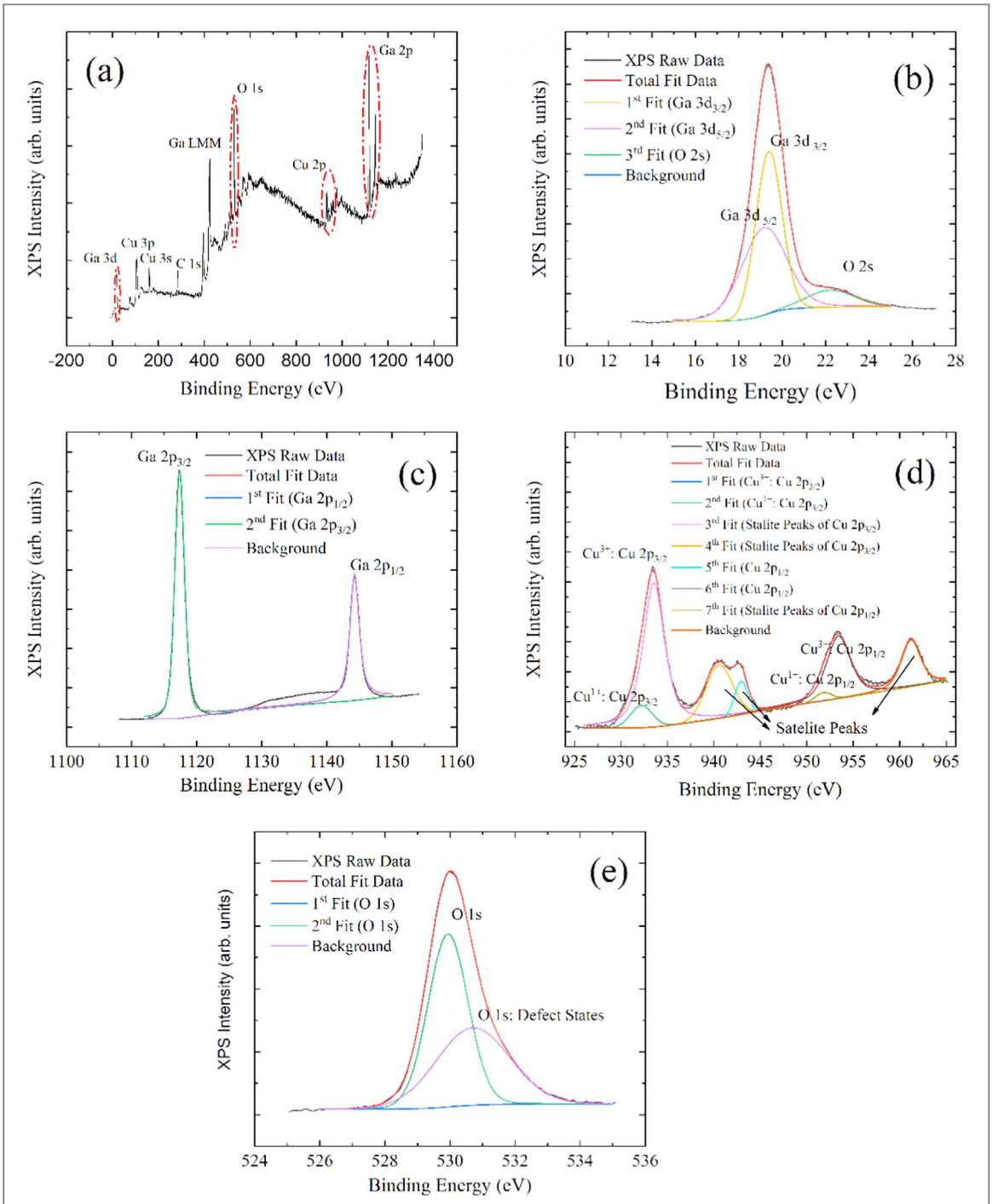


**Figure 5.** XPS spectra of (a) full range, (b) Ga 3d, (c) Ga 2p, (d) Cu 2p and (e) O 2s binding energy levels.

**Table 1.** Calculated band gap values and lattice parameter of $CuGa_2O_4$ particles.

| Sample name | R-bragg factor | 'a' parameter (Å) | 'a' parameters in literature (Å) | Band gap (eV) | Band gap values in literature (eV) |
|---|---|---|---|---|---|
| $CuGa_2O_4$ (annealed at 800 °C) | 1.30 | $8.2992 \pm 0.0001$ | $8.2985 \pm 0.0004$ – $8.2945 \pm 0.0004$ [19] | 2.82 | 2.5–2.6 [7] |
| $CuGa_2O_4$ (annealed at 1000 °C) | 1.32 | $8.3040 \pm 0.0002$ | | 2.86 | |

with electromagnetic emission due to excited electrons from O 1s to Cu 2p energy levels [19]. The bands in range of 700 nm and 1100 nm was originated from d–d transitions due to distorted octahedral geometry around $Cu^{2+}$ ions [19]. On the other hand, the band gap calculations were performed by the peak in range of 200 nm

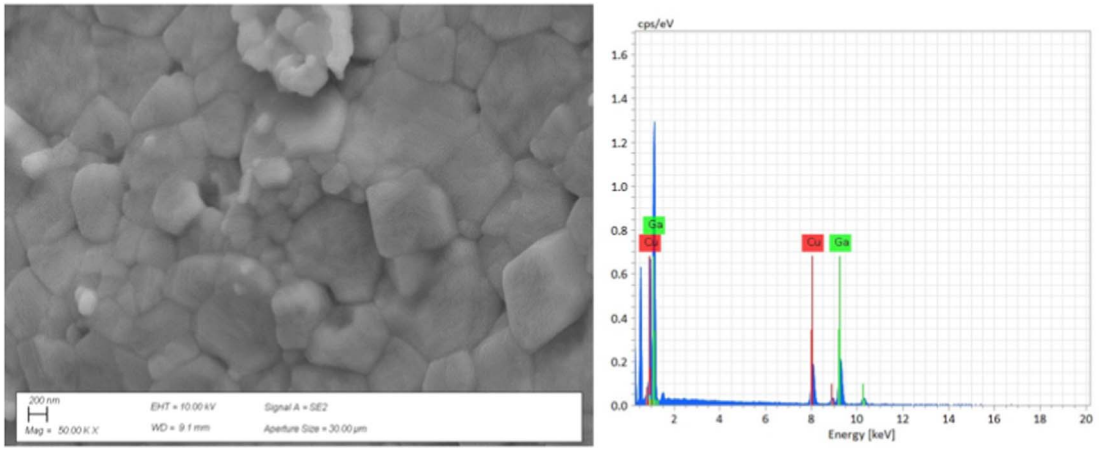


799

| Element | At. No. | Netto | Mass [%] | Mass Norm. [%] | Atom [%] | abs. error [%] (1 sigma) | rel. error [%] (1 sigma) |
|---|---|---|---|---|---|---|---|
| Cu | 29 | 3388 | 25.26 | 32.43 | 34.50 | 0.86 | 3.40 |
| Ga | 31 | 4314 | 52.62 | 67.57 | 65.50 | 1.73 | 3.29 |
| | | Sum | 77.88 | 100.00 | 100.00 | | |

**Figure 6.** Scanning electron microscopy (SEM) micrograph and energy dispersive x-ray scattering (EDS) results of $CuGa_2O_4$ particles obtained at 1000 °C.

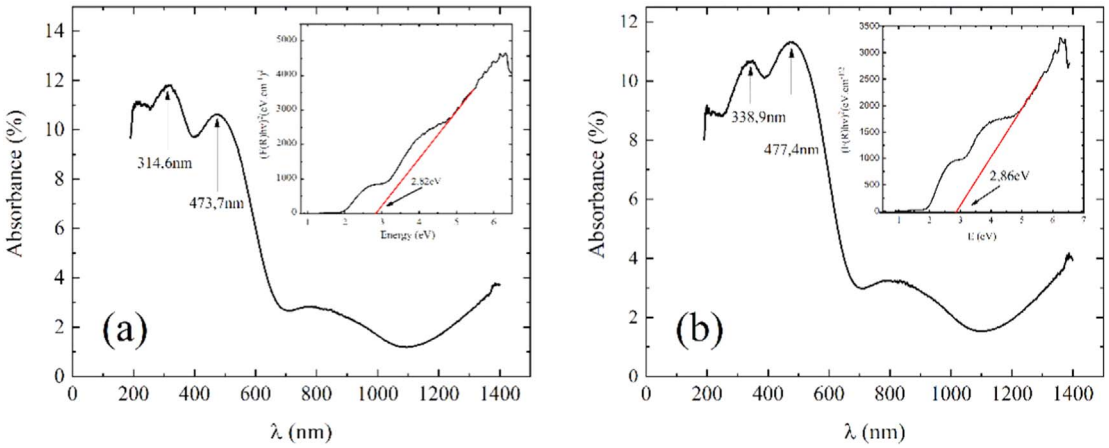


**Figure 7.** UV-Visible photo spectroscopy analyses of $CuGa_2O_4$ particles, annealed at (a) 800 °C and (b)1000 °C.

and 250 nm. The inset figure of absorption spectra shows transformed of absorbance spectra to Kubelka–Munk function (F(R)) versus energy (hν) curve to calculate the optical band gap [6]. The optical band gap calculations were performed for direct transitions.

The band gap values were calculated as 2.82 eV and 2.86 eV for the sample annealed at 800 °C and 1000 °C, respectively. As stated in previous studies, reducing the microstrain caused a decrease in lattice dislocation density and as the consequence of low microstrain, a higher band gap value occurred for sample annealed at 800 °C due to lattice extension of annealed sample at 1000 °C as reported in previous studies. [16, 17, 27].

After understanding the structural formation, particle size distribution and optical transmittance of samples, the $CuGa_2O_4$ particles were arranged as slurry for coating as thick film by tape casting technique. $CuGa_2O_4$ slurry was coated on 10 × 10 $mm^2$ quartz/ITO substrate and then annealed at 400 °C for 2 h as shown inset of figure 8(a). In figure 8(a), the top figure showed the xrd pattern of quartz/ITO substrate and the bottom one the xrd peaks of $CuGa_2O_4$ films on ITO/quartz substrate. The xrd intensity was scaled in arbitrary unit. As seen on figure 8(a), the film was grow up in polycrystalline structure with coherent pattern to $CuGa_2O_4$ pdf cards of 96-153-6351. The SEM figures of surface were demonstrated shown in figure 8(b).

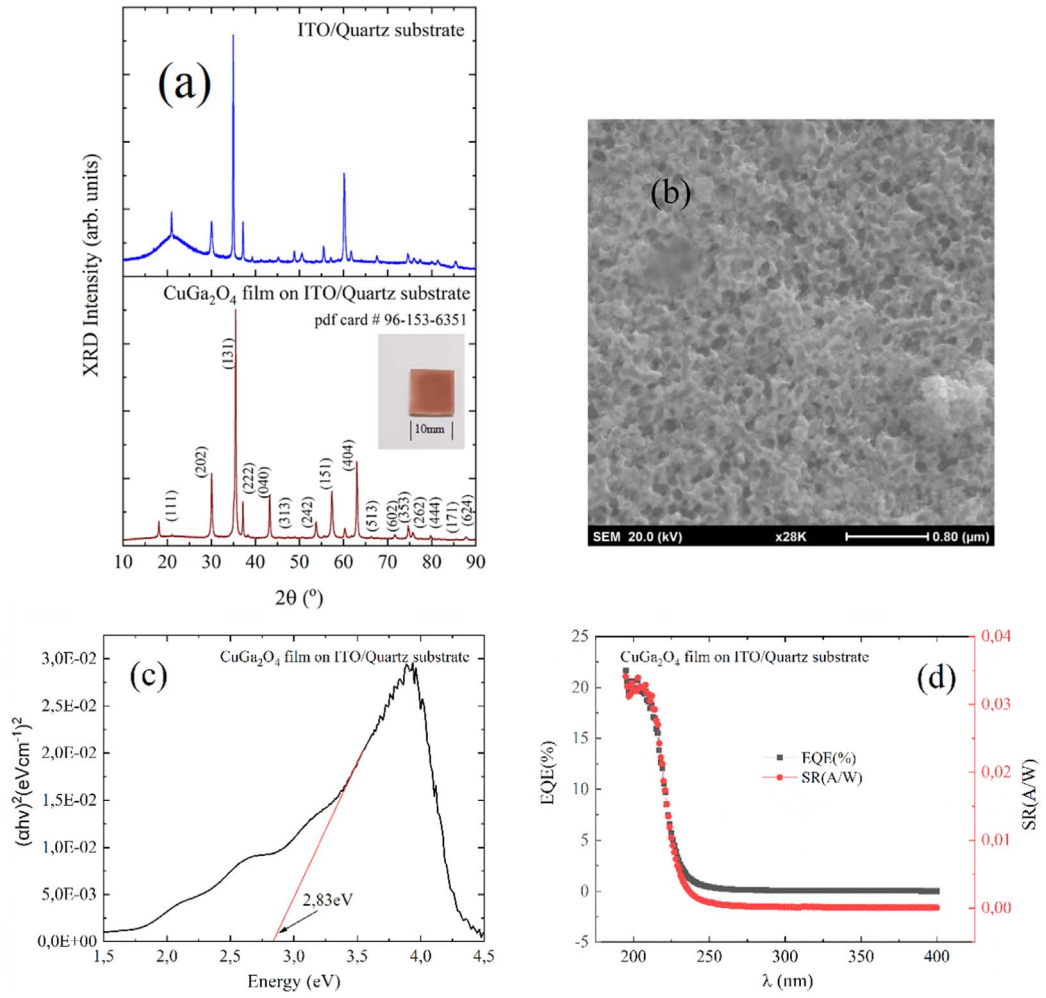


**Figure 8.** (a) x-ray powder diffraction patterns, (b) scanning electron micrographs, (c) UV-Visible photo spectroscopy spectra, and (d) external quantum efficiency (EQE) data of $CuGa_2O_4$ films coated by tape casting technique on ITO/quartz substrate.

As seen on figure 8(b), (a) porous surface was produced with nano sized thick walls, which is suitable to be photo electrode with high surface area. No specific change in band gap, 2.83 eV, of coated film was observed. Then the quantum efficiency was measured to understand the range of wavelength exciting the photo electrodes. As seen in figure 8(d), the photo electrode is effective in UV region of 200 nm and 250 nm with 20% external quantum efficiency in maximum.

## Conclusion

In this study, our primary objective was to synthesize $CuGa_2O_4$ thick films with nano-scale wall thicknesses by integrating the chemical processes of sol–gel and tape casting techniques. The structural analyses revealed that the samples exhibited a typical spinel structure, with a lattice parameter of $8.2992 \pm 0.0001$Å. Additionally, UV-Vis measurements provided insights into the semiconductor properties of $CuGa_2O_4$ spinel oxide. Subsequently, the powders were applied onto quartz/ITO substrates, revealing a noteworthy maximum quantum efficiency of 20% within the UV range of 200 to 250 nm. This study contributes valuable information regarding the fabrication and properties of $CuGa_2O_4$ thick films, paving the way for potential applications in diverse photocatalytic technological fields.

## Acknowledgments

The authors would like to thanks Dr Barış Yağcı for the help at x-ray photoelectron spectroscopy (XPS) measurements. This work was supported by the Scientific Research Projects Coordination Unit of Istanbul

University (Grant No. FDK-2023-39666) and the Scientific and Technological Research Council of Turkey (TÜBİTAK) (Grant No. 118F373).

## Data availability statement

No data was used while preparing this article. The data that support the findings of this study are available uponreasonable request from the authors.

## Author contribution

All authors contributed equally.

## Declarations

The authors have no conflicting interests.

## Conflict of interest

The authors declare that they have no known competing financial interests or personal relationships that could have appeared to infuence the work reported in this paper.

## Ethical approval

Not applicable.

## ORCID iDs

Musa Mutlu Can https://orcid.org/0000-0002-6593-3202

## References

[1] Sickafus K E, Wills J M and Grimes N W 1999 *J. Am. Ceram, Structure of Spinel* **82** 3279–92
[2] Kirankumar V S and Sumathi S 2020 Review on photodegradation of organic pollutants using spinel oxide *Mater. Today Chem.* **18** 100355
[3] Lin S and Zhang T 2023 Research progress in preparation and application of spinel-type metallic oxides (M ⩾ 2) *J. Alloys Compd.* **962** 171117
[4] Shawuti S, Can M M, Gulgun M A and Firat T 2014 Grain size dependent comparison of ZnO and $ZnGa_2O_4$ semiconductors by impedance spectrometry *Electrochim. Acta* **145** 132–8
[5] Masmali N A, Osman Z and Arof A K 2021 Recent developments in zinc-based two-cation oxide spinels: from synthesis to applications *Ceram. Int.* **47** 2949–62
[6] Can M M, Karaman T and Shawuti S 2020 Optical and structural modification of boron-doped $CoGa_2O_4$ particles *Ceramic International* **46** 13025–32
[7] Kendall O, Melendez L V, Ren J, Ratnayake S P, Murdoch B J, Mayes E L H, van Embden J, Gómez D E, Calzolari A and Gaspera E D 2023 Photoactive p-Type spinel $CuGa_2O_4$ nanocrystals *Nano Lett.* **23** 2974–80
[8] Gurunathan K, Baeg J-O, Lee S M, Subramanian E, Moon S-J and Kong K-J 2008 Visible light active pristine and Fe3+ doped $CuGa_2O_4$ spinel photocatalysts for solar hydrogen production *Int. J. Hydrogen Energy* **33** 2646–52
[9] Zhao Q-M, Zhao Z-Y, Liu Q-L, Yao G-Y and Dong X-D 2020 Delafossite $CuGaO_2$ as promising visible-light-driven photocatalyst: synthesize, properties, and performances *J. Phys. D: Appl. Phys.* **53** 135102
[10] Li L, Chen G, Shao Z and Huang H 2023 Progress on smart integrated systems of seawater purification and electrolysis *Energy Environ. Sci.* **16** 4994–5002
[11] Li Y *et al* 2023 Tailoring the surface cation configuration of ruddlesden-popper perovskites for controllable water oxidation performance *Energy Environ. Sci.* **16** 3331
[12] Seshadri H, Cheralathan M and Sinha P K 2013 Photocatalytic performance of combustion-synthesized $\beta$ and $\gamma$-$Ga_2O_3$ in the degradation of 1,4-dioxane in aqueous solution, *Res. Chem. Intermed.* **39** 991–1001
[13] Anas S, Mahesh K V, Jeen Maria M and Ananthakumar S 2017 Sol-gel materials for varistor devices ed S Pillai and S Hehir *Sol-Gel Materials for Energy, Environment and Electronic Applications. Advances in Sol-Gel Derived Materials and Technologies* (Springer) 23–59
[14] Rodriguez-Carvajal J 1993 Recent advances in magnetic structure determination by neutron powder diffraction *Physica* B **192** 55
[15] Pilliadugula R, Nithya C and Krishnan N G 2020 Influence of $Ga_2O_3$, $CuGa_2O_4$ and $Cu_4O_3$ phases on the sodium-ion storage behavior of CuO and its gallium composites *Nanoscale Adv.* **2** 1269
[16] Prabhu Y T, Rao1 K V, Kumar V S S and Kumari B S 2014 X-ray Analysis by williamson-hall and size-strain plot methods of ZnO nanoparticles with fuel variation *World Journal of Nano Science and Engineering* **4** 21–8

[17] Stukowski A, Markmann J, Weissmuller J and Albe K 2009 Atomistic origin of microstrain broadening in diffraction data of nanocrystalline solids *Acta Mater.* **57** 1648–54
[18] Wei H, Chen Z, Wu Z, Cui W, Huang Y and Tang W 2017 Epitaxial growth and characterization of $CuGa_2O_4$ films by laser molecular beam epitaxy *AIP Adv.* **7** 115216
[19] Gingasu D, Mindru I, Patron L, Marinescu G, Tuna F, Preda S, Calderon-Moreno J M and Andronescu C 2012 Synthesis of $CuGa_2O_4$ nanoparticles by precursor and self-propagating combustion methods *Ceram. Int.* **38** 6739–51
[20] Knapp C E, Prassides I D, Sathasivam S, Parkin I P and Carmalt C J 2014 Aerosol-assisted chemical vapour deposition of a copper gallium oxide spinel *Chem Plus Chem* **79** 122–7
[21] Kendall O, Melendez L V, Ren J, Ratnayake S P, Murdoch B J, Mayes E L H, van Embden J, Gómez D E, Calzolari A and Gaspera E D 2023 Photoactive p-type spinel $CuGa_2O_4$ nanocrystals *Nano Lett.* **23** 2974–80
[22] Zardkhoshoui A M and Davarani S S H 2019 Designing a flexible all-solid-state supercapacitor based on $CuGa_2O_4$ and FeP-rGO electrodes *J. Alloys Compd.* **773** 527–36
[23] Faungnawakij K, Shimoda N, Fukunaga T, Kikuchi R and Eguchi K 2008 Cu-based spinel catalysts $CuB_2O_4$ (B = Fe, Mn, Cr, Ga, Al, $Fe_{0.75}Mn_{0.25}$) for steam reforming of dimethyl ether *Appl. Catal., A* **341** 139–45
[24] Sundaresh S, Saikumar A K and Sundaram K B 2022 Investigation on the intermixing of Cu and In Layers for the formation of $Cu_2In_2O_5$ Thin Films *ECS J. Solid State Sci. Technol.* **11** 085003
[25] Yu X, An X, Shavel A, Ibanez M and Cabot A 2014 The effect of the Ga content on the photocatalytic hydrogen evolution of $CuIn_{1-x}Ga_xS_2$ nanocrystals *J. Mater. Chem.* A **2** 12317
[26] Biesinger M C, Lau L W M, Gerson A R, St. R and Smart C 2010 Resolving surface chemical states in XPS analysis of first row transition metals, oxides and hydroxides: Sc, Ti, V, Cu and Zn *Appl. Surf. Sci.* **257** 887–98
[27] Can M M, Akbaba Y and Kaneko S 2022 Synthesis of iron gallate ($FeGa_2O_4$) nanoparticles by mechanochemical method *Coatings* **12** 423